HHS Public Access

Author manuscript

IEEE Trans Ultrason Ferroelectr Freq Control. Author manuscript; available in PMC 2022 July 01.

Published in final edited form as:

IEEE Trans Ultrason Ferroelectr Freq Control. 2021 July ; 68(7): 2516–2531. doi:10.1109/TUFFC.2021.3074113.

Pulse wave imaging coupled with vector flow mapping: A phantom, simulation and in vivo study

Grigorios M. Karageorgos[#], **Iason Z. Apostolakis**[#], **Pierre Nauleau**, **Vittorio Gatti**, **Rachel Weber**, **Paul Kemper**, **Elisa E. Konofagou [Member, IEEE]**

[#] These authors contributed equally to this work.

Abstract

Pulse wave imaging (PWI) is an ultrasound imaging modality that estimates the wall stiffness of an imaged arterial segment by tracking the pulse wave propagation. The aim of the present study is to integrate PWI with vector flow imaging, enabling simultaneous and co-localized mapping of vessel wall mechanical properties and 2-D flow patterns. Two vector flow imaging techniques were implemented using the PWI acquisition sequence: 1) multi-angle vector Doppler, and 2) a cross correlation based vector flow imaging (CC VFI) method. The two vector flow imaging techniques were evaluated in vitro using a vessel phantom with an embedded plaque, along with spatially registered FSI simulations with the same geometry and inlet flow as the phantom setup. The flow magnitude and vector direction obtained through simulations and phantom experiments were compared in a pre-stenotic and stenotic segment of the phantom and at 5 different time frames. In most comparisons, CC VFI provided significantly lower bias or precision than the vector Doppler method ($p<0.05$) indicating better performance. In addition, the proposed technique was applied to the carotid arteries of non-atherosclerotic subjects of different ages in order to investigate the relationship between PWI-derived compliance of the arterial wall and flow velocity in vivo. Spearman's rank-order test revealed positive correlation between compliance and peak flow velocity magnitude ($r_s=0.90$, $p<0.001$), while significantly lower compliance ($p<0.01$) and lower peak flow velocity magnitude ($p<0.001$) was determined in older (54–73 y.o.) compared to young (24–32 y.o.) subjects. Finally, initial feasibility was shown in an atherosclerotic common carotid artery *in vivo*. The proposed imaging modality successfully provided information on blood flow patterns and arterial wall stiffness, and is expected to provide additional insight in studying carotid artery biomechanics, as well as aid in carotid artery disease diagnosis and monitoring.

Keywords

Vector flow imaging; Speckle tracking; Arterial wall stiffness; Pulse wave imaging; Vector Doppler; Vector flow field; FSI simulations; Flow mapping in vivo

I. Introduction

Carotid artery disease is a vascular disease characterized by narrowing of the carotid artery lumen caused by the buildup of atherosclerotic plaques. Carotid artery disease is a major cause of morbidity and mortality, as it often progresses without symptoms, and may go unnoticed until blood supply to the brain becomes limited, causing a transient ischemic attack, or stroke [1][2]. In current clinical practice, there are no reliable biomarkers

associated with early detection of this condition [3]. Moreover, the risk for stroke is primarily evaluated based on the degree of stenosis. This criterion, however, is not highly reliable, since low stenotic plaques may also cause damage [4].

Mechanical properties of the arterial wall may yield crucial information on atherosclerosis initiation [4][5][6]. Key factors contributing to the appearance of carotid artery disease such as vascular aging and hypertension have been associated with increased arterial wall stiffness [7][8]. Moreover, the mechanical properties of an atherosclerotic plaque can provide information on the presence of vulnerable components and thus its risk for rupture and stroke occurrence[9][10]. Ultrasound elasticity imaging techniques may serve as a tool to non-invasively characterize arterial wall properties. Vascular Elastography [11][12][13][14][15][16][17], Shear Wave Elastography (SWE) [18][19][20], Acoustic Radiation Force Imaging (ARFI)[9] and Pulse Wave Imaging (PWI) [21][22][23][24][25][26][27][28] are examples of ultrasound elasticity imaging methods that have shown great promise in vascular disease diagnosis and monitoring.

Blood flow patterns have been reported to precipitate changes in the mechanical properties of the arterial wall and often lead to arterial dilation or stenosis [29][30]. Color Doppler imaging techniques have been investigated to image the hemodynamics in vessels, in order to monitor vascular wall degeneration and vascular disease progression [31][32][33]. Moreover, in current clinical practice, risk assessment of atherosclerosis is primarily based on Duplex and Triplex ultrasound, which provide simultaneous flow imaging and B-mode display [2]. However, those imaging modalities present limitations, given that only 1-D flow velocity estimates are provided to describe more complex flow patterns, while also conventional line-by-line reconstruction highly compromises temporal resolution and/or field of view [34]. Furthermore, the beam-to-flow angle is required in order to convert flow velocity estimates to actual 1-D velocity components, which may introduce bias in the flow estimation, especially in more complex vessel geometries. To address such limitations several methods have been proposed to provide more reliable, angle independent estimation of 2-D flow vector field such as crossbeam vector Doppler [35][36][37], speckle tracking based methods [34][38][39][40] and transverse oscillations [41][42][43][44][45].

Given the importance of vessel wall mechanical properties and blood flow dynamics, as well as the interaction between them in vascular disease progression, it would be desirable to develop an ultrasound modality that provides simultaneous imaging of arterial stiffness and robust 2-D flow velocity estimation [46]. Advances in parallel beamforming and plane wave imaging have shown great promise towards addressing limitations in ultrasound elasticity and flow imaging techniques, as the conventional tradeoff between frame-rate, region of interest and imaging quality is no longer valid, thus producing full field-of-view displacement and Doppler images at high frame rates [47][48]. A method for simultaneous vector Doppler and wall displacement imaging was presented in [47]. The performance of this technique was evaluated in simulations in a carotid bifurcation model and was shown to be feasible in the carotid arteries of healthy volunteers. Another technique is presented in [49], where a single plane wave transmission sequence at 0° was employed, and arterial wall strains as well as 2-D flow vectors were reconstructed through 2-D cross-correlation. This technique was evaluated in a carotid bifurcation phantom, and it was suggested that the use

of high frequency ultrasound circumvents the compromised spatial resolution entailed by the use of single plane wave imaging.

Recently, techniques for simultaneous estimation of PWV and vector flow imaging have been proposed [50][51][52]. In those studies either a single plane wave or a 2-plane wave compounding sequence was utilized. Wall motion was estimated based on the phase shift of the received signals' complex autocorrelation function, while the transverse oscillation (TO) approach was used for vector flow imaging. Clinical feasibility of the proposed technique was recently demonstrated in [52]. In addition, a recent study employed tissue Doppler, combined with multiangle vector Doppler to investigate large artery stiffness and flow patterns in bicuspid aortic valve patients in vivo [53].

The aforementioned studies have shown promising results in phantoms and in-vivo, however, there are multiple other approaches that can integrate vessel wall stiffness mapping with vector flow imaging warranting further exploration. PWI is an example of such techniques, which has been extensively investigated and optimized for PWV estimation in phantoms and in vivo [21][22][23][24][25][26][27]. PWI involves imaging of an arterial segment at high temporal resolution, usually by using a 3- or 5- plane wave compounding acquisition sequence. Subsequently, a speckle tracking technique on the back-scattered RF signals is applied, in order to image the propagation of the distension pulse wave. PWI has been shown capable of monitoring the progression of focal vascular disease such as atherosclerosis [4][5] and abdominal aortic aneurysm [54] in mice, while a more recent study demonstrated its feasibility to differentiate plaques with varying degrees of calcification in carotid artery disease patients [55][56].

The aim of the present study was to integrate PWI with vector flow imaging. Two vector flow imaging techniques were tested, that can be implemented using the PWI acquisition sequence: 1) multi-angle vector Doppler, and 2) a cross correlation based vector flow imaging method. The performance of the two methods was evaluated *in vitro* using a vessel phantom with a stenotic segment, along with spatially registered Fluid Structure Interaction (FSI) simulations with the same geometry and inlet flow as the phantom setup. The same technique was also applied to the carotid arteries of non-atherosclerotic subjects of different age in order to investigate correlations between PWI derived arterial wall compliance and flow velocity in vivo. Finally, initial feasibility was shown in an atherosclerotic carotid artery *in vivo*. It should be noted that this paper is an expansion of a study presented at the 41st Annual International Conference of the IEEE Engineering in Medicine and Biology Society (EMBS), 2019 [57].

II. Materials and Methods

A. Phantom experimental setup

The same experimental setup as in [58] was employed, where the capability of a finite element FSI approach to estimate the velocity of a distension pulse wave propagating through a stenotic artery was investigated. A mold was designed in Autodesk inventor (Autodesk, San Rafael, CA, USA) and 3-D printed (MakerBot, New York, NY, USA) in order to create a phantom with length, inner diameter and wall thickness of 150 mm, 8

mm and 2 mm, respectively. The phantom wall was thicker than a normal artery in order to withstand the pressure load. An ellipsoidal inclusion with 15 mm length was designed 78 mm away from one end of the phantom, in order to mimic the geometry of an atherosclerotic vessel with approximately 50% maximum reduction of luminal area. A polyvinyl alcohol (PVA) mixture was formed by mixing distilled water, PVA powder (Sigma-Aldrich, St. Louis, MO, USA), glycerol and graphite acoustic scatterers (Sigma-Aldrich, St. Louis, MO, USA) at concentrations of 78%, 10%, 10% and 3%, respectively, heated at 90 °C for approximately 40 minutes. Subsequently, the mixture was cooled and then poured inside the 3-D printed mold, and was then subjected to three cycles of freezing (12 h at −20 °C) and thawing (12 h at room temperature). The resulting elastic phantom was then placed inside a custom designed container, and its two ends were connected to plastic fittings. The container was filled with porcine-skin gelatin (Sigma-Aldrich, St. Louis, MO, USA), to serve as the vessel phantom's surrounding medium. The Young's modulus of the PVA material was determined to be E_{PVA}= 42.2 kPa by using a compliance inflation test. A complete description of the experimental and computational procedures to determine the mechanical properties of the materials can be found in [58].

A programmable physiological flow pump (Compuflow 1000, Shelley Medical Imaging technologies, Ontario, Canada) was connected to the fittings of the phantom and was programmed to apply a physiological carotid artery flow waveform, with an amplitude of 10 mL/s, as illustrated in Figure 1. The blood-mimicking fluid described in [59], with nylon scattering particles, and viscosity of 4 mPas was employed. A long time interval equal to 1.9 s was set between consecutive pulses to allow for pulse wave reflections from previous cycles to diminish before the beginning of a new cycle. A pressure catheter (MPR-500, Millar, Houston, TX, USA) was inserted inside the phantom lumen using a cross connector, in order to obtain the temporal waveform of the pressure at the outlet.

The ultrasound probe was attached to a positioner and a layer of water was added to ensure acoustic coupling. Acquisitions were performed along the longitudinal axis of the phantom at two different sites, as shown in Figure 1, by using the inlet of the phantom as reference: Site 1: pre-stenotic straight segment (blue rectangle), and Site 2: stenotic segment centered at FOV (green rectangle).

B. FSI Simulations

FSI simulations were carried out similarly as in [58], using the software suite FEBio [60][61]. The 3-D CAD model of the phantom geometry was converted to FE model using Abaqus CAE (v6.13, Dassault Systèmes). The model was separated into a fluid space, which corresponded to the phantom lumen, and a solid space, which included the arterial wall and the gelatin surrounding medium. The mesh was generated by employing a combination of quadratic tetrahedral (10-node) and pentahedral (15-node) elements using an adaptive meshing algorithm. A maximum node-to-node distance of 0.5 mm for the meshing algorithm was determined with a convergence study. The model had a total of 85,000 elements and 720,000 degrees of freedom.

Appropriate boundary conditions were applied to restrict the motion on the outer surfaces of the surrounding material and the outer surface of the inlet and outlet seLCYctions of

the arterial model. In addition, zero-fluid velocity was set as boundary condition at the outermost surface of the lumen. The same flow waveform as the one generated by the programmable pump, shown in figure 1, was imposed at the inlet of the phantom model. Conversion from mL/s to cm/s was performed using the formula:

$$v_{inlet}\left(\frac{cm}{s}\right) = \frac{v_{inlet}\left(\frac{mL}{s}\right)}{\pi * \left(\frac{D(t)}{2}\right)^2} \quad (1)$$

Where D(t) is the time varying diameter of the phantom lumen at the site of the inlet, and was derived using our ultrasound measurements as described in section II-E-1. The pressure temporal waveform measured by the pressure catheter was imposed at the outlet of the phantom in order to approximate the experimental conditions.

A slightly compressible Newtonian viscous fluid was used to simulate the blood mimicking liquid used for the phantom experiments with a mass density, shear viscosity and bulk modulus of 1060 kg/m^3, 0.004 Pa s and 2 GPa, respectively. The phantom wall was simulated as a homogenous isotropic nearly-incompressible quasilinear viscoelastic material, while the surrounding gelatin was approximated as a homogenous isotropic compressible quasilinear viscoelastic material with a neo-Hookean elastic response. Parameters involving the structural properties of the PVA and gelatin materials (i.e. elastic constants, viscoelastic coefficients) were experimentally determined. A complete description of the structure part of the simulation can be found in [58].

The simulated flow velocity components along the axial ($v_{z,sim}(z, x, t)$) and lateral direction ($v_{x,sim}(z, x, t)$) at each node on the central 2-D slice of the phantom lumen were exported and then post-processed in MATLAB 2017b (Mathworks Inc, Natick, MA, USA).

C. In vivo study

The common carotid arteries of N=10 subjects (24–73 y.o., 8 M, 2 F) and the carotid bifurcation of N=1 subject (24 y.o., F) with no prior history of carotid artery disease were scanned *in vivo*. The subjects were divided into two groups based on their age: N=5 young subjects (24–32 y.o., 5 M) and N=5 older subjects (54–73 y.o., 3 M, 2 F). In order to provide in vivo validation of the proposed vector flow imaging technique, pulsed wave Doppler scan was carried out in one subject (28 y.o., M), using a Siemens Acuson S2000 ultrasound scanner, equipped with a 9L4 Linear array (Siemens, Munich, Germany). The clinical scan was performed immediately after the plane wave compounding scan, at the middle level of the common carotid artery by using the carotid bifurcation as reference, with the subject laying in the supine position. The ultrasound equipment was operated by the same expert sonographer in each case.

In addition, the common carotid artery of one carotid artery disease patient (68 y.o., M) was scanned presenting less than 50 % degree of stenosis, with a calcified plaque as indicated by CT scan examination. All procedures pertinent to the human study were approved by the Human Research Protection Office (HRPO) and Institutional Review Boards (IRBs) of

Columbia University (protocol AAAR0022). Signed consent form was obtained from all subjects before performing ultrasound scans.

D. Ultrasound acquisitions

A Verasonics Vantage 256 research platform (Verasonics, Bothell, WA, USA) was used to drive an L7–4 Linear array transducer with 128 elements, center frequency 5 MHz and 60% Bandwidth (L7–4, ATL Ultrasound, Bothell, WA, USA). A 3-plane wave spatial compounding acquisition imaging sequence, involving the transmission of 3 plane waves at angles θ_e (−10°, 0°, 10°) was implemented at a pulse repetition frequency of 10000 Hz. This particular acquisition sequence was chosen, because it has shown to meet the requirements for temporal resolution and imaging quality to perform PWI processing[25], while also it provides sufficiently large angles for vector Doppler imaging. The sequence was calibrated so that it satisfies the FDA safety guidelines prior to performing in vivo scans. The parameters involving ultrasound acquisitions are summarized in TABLE I.

E. Data post-processing

1) PWI processing—A similar methodology as in [25] was employed to track the distension pulse wave propagation. The received channel data for each transmission angle θ_e, were beamformed separately with a GPU-accelerated version of the delay and sum algorithm, using the respective steering angle on receive [25]. The beamformed RF frames were coherently summed, producing compounded RF frames. The F-number used in the beamforming process was 1.7, and apodization on receive was implemented using a Hanning filter. The axial and lateral resolution of the beamforming grid was 0.01848 mm and 0.2980 mm, respectively. This resolution was chosen because it has shown to provide high quality of pulse wave imaging.

Estimation of the axial wall velocities was performed using a parallel implementation of the 1-D cross-correlation sumtable method [24][25]. The anterior and posterior walls were manually segmented producing thus the axial wall velocity temporal waveforms of the anterior and posterior walls at each lateral position ($v_{anterior,i}(t)$, $v_{posterior,i}(t)$, i=1,2,…,128). The waveforms of the posterior wall were then subtracted from the waveforms of the anterior wall, producing thus the distension rate at each lateral position of the imaged vessel ($v_i(t)= v_{anterior,i}(t) - v_{posterior,i}(t)$, i=1,2,…,128). A Butterworth low pass filter with a cutoff frequency of 30 Hz was applied on $v_i(t)$ in order to suppress high frequency noise that does not correspond to arterial wall motion [62][63]. Subsequently, the axial wall acceleration waveform was derived by performing temporal differentiation ($\alpha_i(t)=dv_i(t)/dt$). The time of arrival of peak $\alpha_{pwi}(t)$, corresponding to the systolic foot of the cardiac cycle (T_{peak}), was calculated at each lateral position. PWV was then estimated as the inverse of the slope of the linear fit applied to consecutive T_{peak} versus lateral position. The acceleration waveform was chosen, because it has been reported to provide more robust pulse wave tracking [64][63]. Figure 2 illustrates an example of an acceleration spatiotemporal plot, along with the linear fit applied for PWV estimation.

The arterial wall compliance was estimated by using the Bramwell-Hill equation as follows:

$$C_k = \frac{\pi\left(\frac{\min(D(t_{ES}))}{2}\right)^2}{\rho(PWV)^2} \quad (2)$$

where $D(t_{ES})$ is the average vessel diameter at the time frame of early systole as obtained through manual wall segmentation, and ρ is the density of blood assumed to be equal to 1060 kg/m^3.

In the case of the carotid artery disease patient, due to the presence of spatial inhomogeneities along the arterial wall, adaptive PWI was employed [5][56]. Adaptive PWI is an extension of PWI developed by our group, which analyzes the arterial wall distension and optimally partitions the artery into the segments with most homogeneous properties, providing thus more robust piecewise compliance estimates.

2) Vector Doppler imaging—The multi-angle vector Doppler approach (Figure 3) described in [35] was employed for vector flow imaging, using the same RF data as in the case of PWI processing. The RF data acquired from each transmission angle $\theta_e \in \{-10°, 0°, 10°\}$ were separately in-phase and quadrature (IQ)-demodulated and subsequently clutter filtered, producing thus a sequence of filtered 2-D IQ frames $IQ_{filt,\theta_e}(z, x, t_{RF})$, where z and x denote the axial and lateral position, respectively, while t_{RF} denotes the time axis of the RF sequence. A spatiotemporal clutter filter based on singular value decomposition (SVD filter) of the ultrasound data was employed to filter the contribution of wall motion on blood flow velocity estimation [65]. A more detailed description of the filtering approach is provided in the Appendix. The $IQ_{filt,\theta_e}(z, x, t_{RF})$ sequence was then divided into ensembles of 40 frames (i.e. ~12 ms) with 90% overlap so that the resulting color Doppler frame sequence would have a frame rate of 833 Hz. Thus, the mean frequency $\left(f_{D,\theta_e}(z, x, t)\right)$ of the power Doppler spectrum for each position, (z,x), and for each ensemble (t) was calculated as follows:

$$f_{D,\theta_e}(z, x, t) = \frac{\int f\left|IQ_{filt,\theta_e}(z, x, t_{RF})e^{-2\pi f t}dt\right|^2 df}{\int\left|IQ_{filt,\theta_e}(z, x, t_{RF})e^{-2\pi f t}dt\right|^2 df} \quad (3)$$

By decomposing the true blood flow velocity vector ($\boldsymbol{v}(z, x, t)$) into a vector along the axial direction ($v_z(z, x, t)$) and one along the lateral direction ($v_x(z, x, t)$) and using the revised form of the Doppler equation [36] [66] we have the following system of equations:

$$\begin{aligned} v_z(z, x, t) * (\cos(\theta_e) + 1) + v_x(z, x, t) * \sin(\theta_e) \\ = \frac{c}{f_c} f_{D,\theta_e}(z, x, t) = v_{\theta_e}(z, x, t) \end{aligned} \quad (4)$$

where θ_e, $t \in \{1, 2, 3\}$ is the transmission angle of the plane wave, f_c is the center frequency of the ultrasound, c is the speed of sound, and $v_{\theta_e}(z, x, t)$ indicate the estimated Doppler blood velocities, respectively, for the tilted plane wave transmission at an angle θ_e. Thus, a system with three equations and two unknowns was created for each point on the

Doppler images and was solved in parallel for all the image points using a GPU-enhanced least-squares solver:

$$\begin{bmatrix} v_x(z,x,t) \\ v_z(z,x,t) \end{bmatrix} = A^{+} \begin{bmatrix} v_{\theta_{e1}}(z,x,t) \\ v_{\theta_{e2}}(z,x,t) \\ v_{\theta_{e3}}(z,x,t) \end{bmatrix} \tag{5}$$

where A^{+} is the pseudoinverse matrix of A, the matrix containing the steering angles:

$$A = \begin{bmatrix} \sin\theta_{e1} & \cos\theta_{e1} + 1 \\ \sin\theta_{e2} & \cos\theta_{e2} + 1 \\ \sin\theta_{e3} & \cos\theta_{e3} + 1 \end{bmatrix} \tag{6}$$

The resulting flow velocity components (v_X and v_Z) were spatially filtered by using a 2-D median kernel of 7×7. Subsequently, the magnitude of the derived velocity vectors was color-coded and overlaid onto the B-mode. To visualize the direction of the velocity vectors, a vector field was overlaid on top of the color-coded magnitude of the velocities. The axial wall velocities were also overlaid onto the B-mode.

3) Cross-correlation vector flow imaging—Cross-correlation vector flow imaging (CC VFI) was employed using a similar approach as in [67], where speckle tracking is used to track the 2-D motion of blood scatterers (Figure 4). The compounded RF signals were clutter filtered using the same SVD filter as in section II-E-2), aiming to eliminate the slow motion of the arterial wall, and enhance the RF signals obtained from blood flow. A 1D normalized cross correlation kernel was subsequently applied on consecutive filtered RF frames in a 2-D search, using a kernel overlap of 1 axial sample (0.01848 mm), in order to estimate the inter-frame displacements at each point location in the field of view [68]. The size of the kernel was set at 40 (0.7392 mm) axial samples in the case of the phantom study and 80 (1.4784 mm) for the in vivo study. To increase the accuracy of displacement estimates, a 10:1 linear interpolation was performed between adjacent RF lines [69]. The resulting inter-frame displacements were then normalized by the frame rate in order to obtain the axial ($v_Z(z, x, t)$) and lateral ($v_X(z, x, t)$) flow velocity components. The maximum search range was set at 7 samples (0.1294 mm, maximum velocity: 43.13 cm/s) across the axial and 3 samples (0.8940 mm, maximum velocity: 298.0 cm/s) across the lateral direction. The resulting flow velocity components were averaged in temporal ensembles of 40 frames (i.e. ~12 ms) with 90% overlap, in order to obtain the same vector flow imaging frame rate as in the vector Doppler approach. Finally, the same spatial filter as in the vector Doppler approach was applied on v_X and v_Z (2-D median kernel of 7×7).

4) Vector flow imaging performance evaluation—In the case of the phantom study, each vector flow imaging frame was spatially registered with the corresponding simulated vector flow field by using the inlet of the phantom as reference. Interpolation was performed along the lateral (x-axis) and axial (z-axis) directions, in order to map the simulated and measured vector flow fields at the same grid of size 128 and 80 samples along the x- and z-axis, respectively. The lateral resolution (0.298 mm) of the resulting grid was chosen to

match the ultrasound field of view, while the axial resolution (0.1 mm) was selected to account for the minimum node-to-node distance of the FSI simulation. The flow velocity magnitude ($v_m(z, x, t)$) and vector flow angles ($\theta(z, x, t)$) were calculated at each point location (z,x) and time frame (t) as follows:

$$v_m(z,x,t) = \sqrt{v_z^2(z,x,t) + v_x^2(z,x,t)} \tag{7}$$

$$\theta(z,x,t) = tan^{-1}\left(\frac{v_z}{v_x}\right) \tag{8}$$

The flow velocity profile obtained through each one of the two vector flow imaging methods was compared to the simulated one, by calculating the bias (B) and precision (σ) of flow velocity magnitude and vector angles across the axial direction (z) at each lateral position, and then averaging across the lateral direction (x):

$$B_{v_m}(t) = AVG_x\left\{\frac{1}{v_{sim,max}(x,t)} AVG_z\{\,|\, v_{m,sim}(z,x,t) - v_{m,vfi}(z,x,t)\,|\,\}\right\} \tag{9}$$

$$B_\theta(t) = AVG_x\left\{AVG_z\left\{\left|\theta_{sim}(z,x,t) - \theta_{vfi}(z,x,t)\right|\right\}\right\} \tag{10}$$

$$\sigma_{v_m}(t) = AVG_x\left\{\frac{1}{v_{sim,max}(x,t)} STD_z\{\,|\, v_{m,sim}(z,x,t) - v_{m,vfi}(z,x,t)\,|\,\}\right\} \tag{11}$$

$$\sigma_\theta(t) = AVG_x\left\{STD_z\left(\left|\theta_{sim}(z,x,t) - \theta_{vfi}(z,x,t)\right|\right)\right\} \tag{12}$$

Where the subscripts “sim” and “vfi”, “v_m”, and “θ”, stand for simulation, vector flow imaging, flow velocity magnitude and vector flow angles, respectively. $AVG_{(z,x)}\{\}$ and $STD_z\{\}$ denote the averaging and standard deviation operators along the axial (z) or lateral (x) direction, respectively, and $v_{sim,max}(x, t)$ is the maximum value of the simulated axial velocity profile for a given lateral position and time frame. Division with $v_{sim,max}(x, t)$ was performed to express the flow velocity magnitude bias and precision in relative quantities.

Averaging across the lateral direction was performed in two regions as illustrated in Figure 5 – (a): i) entire FOV (x∈ [0, 37.8 *mm*]) and ii) plane wave overlapping zone FOV (x∈ [6.2, 31.6 *mm*]) where all three plane waves overlap. The latter region was chosen, because the transmitted plane waves are tilted at angles (−10°, 0°, 10°), thus, flow measurements are expected to be less accurate towards the edges of the field of view, where only 2 out of three plane waves overlap. The plane wave overlapping zone is function of depth (z-axis) and its distance from the first and last lateral positions is given as $d_{overlap}$ = z*tan(10°). In the case of the phantom study, this distance was calculated for the maximum depth of the phantom lumen and was determined to be $d_{overlap}$=6.2 mm.

Bias and precision values were calculated at five different temporal samples as shown in Figure 5–(b): T_0, T_{25}, T_{50}, T_{75} and T_{100} which correspond to the foot, 25%-, 50%-, 75%-upstroke points and peak of the flow velocity waveform, respectively.

The bias and precision in magnitudes and angle (B_{v_m}, B_θ, σ_{v_m}, σ_θ), obtained through vector Doppler and CC VFI were compared separately at the pre-stenotic and stenotic segments, by using a paired t-test among different time frames (total of 8 comparisons, N=5 per comparison).

III. Results

A. Simulation and phantom study

Figure 6–(a) illustrates the 2-D flow at the time frame of peak systole (T_{100}), corresponding to the central 2-D slice of the phantom's geometry, as obtained through FSI simulation. The blue and green rectangles denote the pre-stenotic and stenotic segments, respectively (as described in section 2.1 - Figure 1). Figure 6–(b),(c),(d) demonstrate the peak systolic vector flow field in the pre-stenotic segment obtained through simulation, vector Doppler and CC VFI, respectively. Figure 6–(e),(f),(g) demonstrate the corresponding vector flow fields in the stenotic segment. It can be observed that the CC VFI method provided smoother flow velocity magnitude images as compared to vector Doppler, which qualitatively approximates better the simulated vector flow field.

Figure 6–(h),(i) show the axial flow velocity magnitude profiles at the foot (T_0) and peak (T_{100}) time frames as obtained through vector Doppler and CC VFI, respectively, in the pre-stenotic segment. Figure 6–(j),(k) illustrate the respective axial flow velocity magnitude profiles in the stenotic segment. The axial flow profiles were extracted from the lateral positions illustrated in blue (Figure 6–(b)) and green (Figure 6–(e)) dashed lines in the pre-stenotic and stenotic segments, respectively, and were interpolated to the same grid as the simulated vector flow field, as described in section II-E-4.

The quantitative performance evaluation results are summarized in Figure 7 and Table-II. Figure 7 illustrates the average bias and precision in flow velocity magnitude (a, b, e, f) and vector angles (c, d, g, h), with respect to the time frame in the pre-stenotic (a - d) and stenotic (e - h) segments. The metrics presented in gray and black lines correspond to the plane wave overlapping zone and the entire FOV, respectively. It can be observed that in each case, both bias and precision are lower in the plane wave overlapping zone, indicating better quality of vector flow imaging in this region for both methods, as compared to the entire FOV.

Table-II summarizes the comparison of the performance metrics between the two vector flow imaging techniques in the plane wave overlapping zone. Each cell of the table presents the mean and standard deviation of each metric across the 5 different time frames. In 4 out of 8 comparisons, paired t-test revealed significantly better performance of the CC-VFI technique (significantly lower σ_{v_m} in the pre-stenotic segment and $\sigma_\theta\sigma_{v_m}B_{v_m}$ in the stenotic segment, $p<0.05$). In the pre-stenotic segment, vector Doppler provided significantly lower B_θ ($p<0.05$), while no significant differences were found in the remaining comparisons.

Those comparisons suggest that CC VFI outperforms vector Doppler in most cases, particularly in the stenotic segment, which is characterized by higher flow velocity. In the case of the pre-stenotic segment, it can be observed in Figure 7–(a),(b) that CC VFI provides higher B_{v_m} than the vector Doppler approach at time frames corresponding to lower velocity values (T_0, T_{25}, T_{50}), and drops at higher velocities reaching a minimum value of 6.89% at T_{100}, with a σ_{v_m} of 5.81%. However, the precision σ_{v_m} of CC VFI remains lower than vector Doppler, indicating less noisy flow velocity magnitude estimates. Both vector flow imaging methods provided similar performance in vector flow angle estimation. Given that CC VFI provided significantly lower precision and bias in most of the comparisons, we choose to integrate PWI with the CC VFI technique.

B. In vivo study

Figure 8–(a) illustrates the PW Doppler results in the middle of the CCA of one healthy subject. Figure 8–(b),(c) show the PWI coupled with CC-VFI image sequence at the same arterial segment as in Figure 8–(a). The illustrated frames correspond to the peak systolic (8–(b)) and end diastolic (8–(c)) phases. Figure 8–(d) shows the Temporal waveform of flow velocity magnitude corresponding to the center of the lumen (green rectangular marker in Figure 8–(b)), which is the approximate location of the PW Doppler measurement. Figure 8–(e) illustrates an alternative display of the proposed method, in which streamlines are plotted onto the B-mode in order to provide improved visualization of the directional flow in the common carotid.

Videos depicting the image sequences have been included as supplemental material. In supplemental material 1, it can be observed that the streamlines align upon arrival of the distension pulse wave, and subsequently follow a trajectory towards the bottom wall. The downward motion of the streamlines can possibly indicate the tendency of blood to flow through the less resistive route at the carotid bifurcation. Supplemental material 2 demonstrates a particle visualization of vector flow imaging, where the red dots follow the motion of blood. A vortex can be seen at the level of the carotid bifurcation.

The peak systolic flow velocity magnitude obtained through CC-VFI was 101.21 cm/s which was in good agreement with the value obtained by the clinical scanner (98.8 cm/s), with a relative error of 2.4%.

Figure 9–(a) and (b) demonstrate the estimated PWV and arterial wall compliance, respectively, versus the peak flow velocity magnitude, averaged along the centerline of the vessel, in each subject (N=10). Spearman's rank-order test revealed significant negative correlation between PWV and peak flow velocity magnitude (r_s=−0.86, $p<0.01$), while positive correlation was observed between carotid wall compliance and peak flow velocity magnitude (r_s=0.90, $p<0.001$). Figure 9–(c), (d) illustrate a comparison of flow velocity magnitude and compliance, respectively, in non-atherosclerotic young and older subjects. Unpaired t-test revealed that subjects in the young group had significantly higher carotid artery compliance, compared to older subjects ($1.76 \pm 0.34 * 10^{-9}$ m^2/Pa versus $0.85 \pm 0.19 * 10^{-9}$ m^2/Pa, $p<0.01$), as well as significantly higher flow velocity magnitude (92.60 ± 6.34 cm/s versus 66.25 ± 4.98 cm/s, $p<0.001$).

Figure 10 shows an example of the proposed method in an atherosclerotic common carotid artery. Figure 10–(a) demonstrates the B-mode image with the flow magnitude and vector field overlaid inside the lumen and the axial wall velocities overlaid on the walls. The orange lines depict the borders of the lumen, obtained through manual wall segmentation. Figure 10–(b) shows the result of adaptive PWI post processing, where the yellow dashed lines indicate the borders arterial segments with most uniform pulse wave propagation. The piecewise compliance values estimated for each segment were color-coded and overlaid onto the B-mode Figure 10–(c) shows the peak flow magnitude along the centerline of the vessel with respect to the lateral position, in a common graph with the lumen diameter, as obtained through wall segmentation. Figure 10–(d) demonstrates the spatiotemporal plot of distension rate ($v_i(t)$) depicting the distension pulse wave propagation. The vertical red dashed line indicates the lateral position where the flow magnitude maximizes, while the green lines indicate the borders of the stenotic segment as determined by analyzing the 2^{nd} derivative of the diameter waveform, using a method described elsewhere [6]. The flow magnitude is shown to reach its maximum approximately at the point of maximum stenosis, while it drops in the post-stenotic segment, which is a similar observation as in the case of the phantom study.

The average compliance estimated by adaptive PWI in the stenotic segment was found to be equal to 0.64 $*10^{-9}$ m^2/Pa, which is low compared to average value in both young (1.76 ± 0.34 $*10^{-9}$ m^2/Pa) and older subjects 0.85 ± 0.19 $*10^{-9}$ m^2/Pa). This can be explained considering that a calcified plaque was present, which is associated with increased stiffness. Moreover, it can be seen in Figure 10–(d) that the amplitude of $v_i(t)$ decreases in the stenotic segment, particularly at lateral positions following the peak flow magnitude. This is possibly an effect of the pressure drop across the plaque, which limits the degree of arterial wall distension rate. Also, reduced degree of distension in the stenotic segment can be linked to plaque calcifications, as supported by another study involving applications of PWI in carotid artery disease patients [55].

IV. Discussion

In this study, PWI was integrated with vector flow imaging, enabling simultaneous and co-localized imaging of arterial wall distension pulse wave propagation and blood flow patterns. The developed imaging modality is expected to provide additional insight in studying carotid artery biomechanics, and aid in carotid artery disease diagnosis and monitoring. Two separate vector flow imaging techniques, vector Doppler and CC-VFI, were implemented using the PWI sequence. The performance of the two techniques was investigated through experiments and simulations in a phantom mimicking the geometry of a stenotic vessel. Furthermore, the feasibility of the proposed method was tested by investigating associations between vessel wall mechanical properties and flow velocity in the common carotid arteries of non-atherosclerotic human subjects. Finally, initial feasibility was presented in an atherosclerotic carotid artery *in vivo*.

Overall, CC-VFI provided lower bias and precision, suggesting better performance than the vector Doppler technique for the given acquisition sequence. A limitation of the Doppler method is the effect of geometrical spectral broadening, which may introduce errors in flow

velocity calculation depending on the beam-to-flow angle [70]. This effect is expected to reduce the quality of the vector Doppler approach employed in this study, given that Doppler spectra are calculated from plane wave emissions with varying beam-to-flow angles, and then combined to reconstruct the 2-D vector flow field. Moreover, ultrasound acquisition parameters such as pulse duration, number and angles of transmitted plane waves were chosen based on an optimization study involving the PWI sequence [25]. However, those parameters may not be optimal for accurate Doppler signal determination, leading to lower quality of Doppler velocity estimates [37]. Alternative implementations of Doppler-based techniques, such as the ones described in [37][71] may provide improved performance for vector flow imaging.

Comparison between a cross correlation and a vector Doppler based approach has also been performed through simulations in [72], where the cross correlation method resulted in more robust mapping of lateral flow velocity. This is consistent with the findings of the present study, with the CC-VFI derived flow velocity magnitude presenting lower bias and precision in most comparisons. However, no significant differences were determined in terms of vector flow angles, which can be attributed to the fact that the vector Doppler technique may provide higher quality of axial flow velocity estimates [72]. Overall, the cross correlation method was considered to provide more advantages for vector flow imaging [72]. Consistent results were reported by a more recent study, where vector Doppler was outperformed by a speckle tracking-based technique used on compounded RF signals, with the latter being less dependent on the beam-to-flow angle, number of transmitted plane waves and RF filtering [34].

It was observed that the bias and precision of CC-VFI obtained higher values at lower flow velocity levels. This can be attributed to the fact that the cross-correlation parameters for blood motion tracking (i.e. kernel size, kernel overlap, interpolation factor and search range) had a fixed value for the entire cycle. Different configurations of those parameters would result in different bias and precision of the proposed technique, for a given flow velocity magnitude. In this study, we experimented with multiple configurations and chose the one that better approximated the simulations, or the clinical Doppler scan in the case of the in-vivo study. Ongoing efforts involve the implementation of an adaptive algorithm that will determine the optimal cross correlation parameters with respect to the phase of the cardiac cycle.

An additional shortcoming of the presented CC-VFI implementation is the application of 2-D speckle tracking in compounded RF frames, consisting of asynchronous plane wave emissions. Coherent compounding is based on the assumption of stationary field of view. However, this assumption is not valid, since blood scaterrers are moving in between different transmissions, resulting in incoherent summation of the backscattered signals. This effect is expected to impact the quality of RF frames, and therefore, flow velocity estimation. This issue can potentially be addressed by employing a motion correction technique on the compounded RF frames, such as the one presented in [35].

Due to technical limitations entailed by the pump and the limited strength of the phantom material, the generated flow waveform provided lower flow velocity values, as compared to

those in a physiological common carotid artery. To validate CC VFI at higher flow velocity levels, the common carotid artery of one healthy subject was scanned in vivo using a clinical scanner, which provided good approximation of the peak systolic velocity.

Another matter warranting further investigation is the maximum flow velocity value that can be estimated using CC-VFI. The upper limit of velocity that can be provided by the multiangle vector Doppler approach is defined by the Nyquist frequency. In the case of CC-VFI, decorrelation is expected to affect the performance of motion tracking when the interframe displacement of blood scatterers is too large, or in case of more complex flow patterns such as vortices. Future work would include the development of an experimental setup that will be able to support higher flow velocity waveforms and more complex flow patterns, to provide a more complete performance evaluation of the proposed technique.

Performance evaluation of vector flow imaging techniques in terms of bias and precision has been previously carried out [37] [41][43][45][73][74][71]. The evaluation approaches used in [41][42] demonstrate more similarities with the methodology employed in this paper, where flow velocity measurements from straight vessel tubes with large diameter and pulsatile excitation, are directly compared with the theoretical vector flow field. According to [41], the transverse oscillation method provided an average bias of axial and lateral flow velocities lower than 20%, with the lateral component providing similar bias and precision values as the ones provided by CC-VFI flow velocity magnitude. An improved version of TO was developed in [42], where the average standard deviation of vector flow angles and lateral velocity was reported to be 2.8° and 9.2%, respectively, while the mean bias in lateral flow velocity was equal to −3.4%. Those values are comparable to the case of CC-VFI in the pre-stenotic segment at peak systole, with a precision in vector flow angles and flow velocity magnitude equal to 1.83° and 5.81%, respectively, and a bias in flow velocity magnitude of 6.89 %. It should be noted that the framework used for performance evaluation in this study provides less idealized flow conditions compared to the aforementioned studies, given that it incorporates pulsatile vessel wall motion both in the phantom experiments and simulations. It is therefore more challenging to achieve low bias and precision values given the complexity added by the structure interaction component.

A similar method for simultaneous vector flow imaging and PWV estimation was presented in [47], where the transverse oscillations (TO) approach was employed. An advantage of TO is that it is a better established approach for vector flow imaging, as compared to the speckle tracking method employed in this study. However TO has not been as extensively investigated for arterial wall stiffness estimation, compared to PWI. A potential advantage of CC-VFI is that it does not require large beam-to-flow angles since it uses axial and lateral speckle tracking on the compounded RF signals, and therefore, it can be easily integrated with various plane wave transmission sequences. It has been demonstrated that the quality of vector flow field mapping provided by TO improves as the beam to flow angles of the transmitted plane waves increase [42], a fact that may compromise the quality of B-mode image and/or displacement estimation.

A limitation of the experimental performance assessment is the effect of pulse pave reflections generated at the outlet of the phantom. When the pulse wave propagates through

a discontinuity in stiffness or cross sectional area, then a reflected wave is generated travelling in the opposite direction. The reflected wave is superimposed with the forward one, affecting the uniformity of flow and pressure waveforms.

To mitigate potential bias introduced by pulse wave reflections, performance evaluation was not carried out at time frames later that the peak systole. That is because the major effect of pulse wave reflections is expected to occur when the wave that corresponds to peak systole is reflected at the outlet and merges with the forward one. Moreover, we did not perform our analysis in the post-stenotic segment of the phantom close to the outlet, which is rather challenging to model accurately due to its proximity to sources of pulse wave reflections. Less accurate modelling in this particular segment was also observed in [58], where a similar analysis was performed to compare simulated with measured PWV values, and a higher error was determined in the post-stenotic segment. Next steps would involve more accurate representation of the outlet boundary condition and reflection generation, by utilizing more sophisticated approaches, such as the Windkessel resistance module described in [75].

The aim of the *in vivo* study in non-atherosclerotic subjects was to support the clinical importance of the proposed technique by investigating associations between two crucial biomarkers of vascular health. Peak systolic flow velocity values provided by CC-VFI are consistent with values reported by previous studies, both for the young and older subjects [76][77][78][79]. Significantly higher compliance and flow velocity magnitude were observed in young subjects compared to older ones. This finding is consistent with previous studies which have reported increased vascular stiffness [6] [52][80] and reduced flow [81][77] with age. Moreover, a significantly positive correlation was determined between arterial wall compliance and peak flow velocity magnitude. The relationship between wall stiffness and blood flow dynamics in human carotid arteries *in vivo* has been previously investigated, with the wall shear stress considered as an important factor in vascular wall remodeling and stiffening [77][82]. However, there has not been a standard technical basis for direct and robust regional wall stiffness and flow velocity vector field estimation, thus, the exact role of hemodynamic forces in arterial wall degeneration remains unclear [83][44]. Ongoing efforts include application of the proposed technique in a larger cohort of human subjects to further investigate dependencies between arterial mechanical properties and blood flow patterns.

Furthermore, initial feasibility of the proposed method was shown in one atherosclerotic subject *in vivo*. A relatively low compliance was determined, which can be justified considering that a calcified plaque was present. It is known that calcifications can increase the plaque's stiffness, and previous application of PWI in atherosclerosis patients has demonstrated its capability in differentiating among plaques with different degree of calcification [55]. Imaging of the atherosclerotic plaque mechanical properties in conjunction with applied hemodynamic forces may yield significant information on vulnerable plaque detection and stroke prevention. Pulse wave velocity and intra-plaque displacements can be utilized to identify structural components associated with increased vulnerability (i.e. high lipid necrotic core, thrombus), while flow vector field can reveal regions of the fibrous cap with increased stress that can be potential sites of rupture. It should be noted that a limitation of the in-vivo study is potential misalignment of the

ultrasound probe with the axis of the common carotid artery, which may introduce bias in peak flow velocity estimation.

A factor that may bias the PWI technique is that only axial wall motion is considered to track the pulse wave propagation. In cases of more complex geometries, i.e. when an atherosclerotic plaque is present, the vessel is not aligned with the lateral direction, and lateral motion is not taken into account. This is not expected to significantly bias PWV estimation, since it based on tracking a temporal feature of the distention waveform, which is expected to occur simultaneously for the axial and lateral components of arterial wall distension. It yet remains to assess the angle independence of PWI in atherosclerotic vessels.

Finally, simultaneous information on flow velocity and wall displacements may enable the development of more sophisticated and robust methods for arterial wall mechanical characterization. The pulse wave inverse problem (PWIP) [84] is an example of such techniques, which provides spatially resolved compliance measurements based on the spatiotemporal variation of arterial wall displacements, while also accounting for effects of pulse wave reflections. However, previous PWIP implementation was based on assumptions regarding the flow velocity profile and boundary conditions, which may introduce errors in compliance estimation. A future step of this work would be to supplement PWIP with simultaneous vector Doppler measurements, in order to enhance its mechanical characterization capabilities.

V. Conclusion

A non-invasive ultrasound imaging technique was presented for simultaneous and co-localized imaging of distension pulse wave propagation and 2-D vector flow field. The accuracy of the proposed technique was investigated *in vitro* using a stenotic vessel phantom and through FSI simulation. Moreover, its feasibility was shown to investigate associations between carotid artery Pulse Wave Velocity and blood flow patterns, *in vivo*. This method is expected to provide more insight in the biomechanical behavior of arteries, aiding thus in vascular disease diagnosis and monitoring.

Supplementary Material

Refer to Web version on PubMed Central for supplementary material.

Acknowledgements

This study was funded in part by the National Institutes of Health: R01HL135734. The authors thank Julien Grondin, Ph.D. and Nirvedh Harshad Meshram, Ph.D. for their helpful contributions.

This work was supported by a grant of the National Institutes of Health (NIH 1-R01-HL135734).

Appendix. Singular Value Decomposition filtering

A singular value decomposition (SVD) filtering approach similar to the one presented in [65] was employed. Let us consider the sequence of beamformed RF frames shown in Figure 11–(a), stacked in a 3-D matrix of size (M_z, M_x, M_t), where M_z, M_x, M_t denote the

number of samples across the depth, width and time axes, respectively (Figure 11–(a)). In this study, the stack includes the full sequence of acquired Rf frames, leading to an M_t of 3999 samples. The first step in the SVD filtering approach is transforming the 3-D stack of RF frames into a 2-D Casorati matrix (S) of dimension (M_x x M_z, M_t). Subsequently, the Casorati matrix is diagonalized and decomposed into a temporal (U) and spatial (V) singular vector basis as follows:

$$S = U\Delta V^*$$

Where Δ is a diagonal matrix with the singular values of S.

The RF signals backscattered from tissue are characterized by high spatiotemporal coherence and correspond to higher singular values, as compared to signals obtained from blood scatterers. The aim of SVD filtering is to reject singular components that correspond to tissue motion by selecting a singular value as a threshold (δ_T). To select the threshold, the GUI shown in Figure 11 was developed. The blue line demonstrates the singular values of Δ in dB, sorted by decreasing singular value. while the vertical red line illustrates the position of the threshold singular value. The arrows allow the user to manually select the position of the red line. In this study, the elbow of the curve was selected as the threshold δ_T that provides separation between tissue motion (high singular values) and blood flow or noise (low singular values). More detailed description involving the SVD filtering approach can be found in [65].

References

[1]. Spence JD, Song H, and Cheng G, “Appropriate management of asymptomatic carotid stenosis,” Stroke and Vascular Neurology, vol. 1, no. 2. BMJ Publishing Group, pp. 64–71, 01-6-2016. [PubMed: 28959466]

[2]. Grotta JC, “Carotid Stenosis,” N. Engl. J. Med, vol. 369, no. 12, pp. 1143–1150, 9. 2013. [PubMed: 24047063]

[3]. Fernández-Ortiz Aet al., “The Progression and Early detection of Subclinical Atherosclerosis (PESA) study: Rationale and design,” Am. Heart J, vol. 166, no. 6, pp. 990–998, 12. 2013. [PubMed: 24268213]

[4]. Apostolakis IZ, Nandlall SD, and Konofagou EE, “Piecewise Pulse Wave Imaging (pPWI) for Detection and Monitoring of Focal Vascular Disease in Murine Aortas and Carotids In Vivo,” IEEE Trans. Med. Imaging, vol. 35, no. 1, pp. 13–28, 1. 2016. [PubMed: 26168432]

[5]. Apostolakis IZ, Karageorgos GM, Nauleau P, Nandlall SD, and Konofagou EE, “Adaptive Pulse Wave Imaging: automated spatial vessel wall inhomogeneity detection in phantoms and in-vivo,” IEEE Trans. Med. Imaging, pp. 1–1, 2019.

[6]. Nichols WW, O’Rourke MF, Vlachopoulos C, and McDonald DA, McDonald’s blood flow in arteries : theoretical, experimental and clinical principles. Hodder Arnold, 2011.

[7]. Sun Z, “Aging, arterial stiffness, and hypertension.,” Hypertens. (Dallas, Tex. 1979), vol. 65, no. 2, pp. 252–6, 2. 2015.

[8]. Avolio AP, Chen SG, Wang RP, Zhang CL, Li MF, and O’Rourke MF, “Effects of aging on changing arterial compliance and left ventricular load in a northern Chinese urban community.,” Circulation, vol. 68, no. 1, pp. 50–58, 7. 1983. [PubMed: 6851054]

[9]. Czernuszewicz TJet al., “Non-invasive in Vivo Characterization of Human Carotid Plaques with Acoustic Radiation Force Impulse Ultrasound: Comparison with Histology after Endarterectomy,” Ultrasound Med. Biol, vol. 41, no. 3, pp. 685–697, 3. 2015. [PubMed: 25619778]

[10]. Lee RTet al., "Prediction of mechanical properties of human atherosclerotic tissue by high-frequency intravascular ultrasound imaging. An in vitro study.," Arterioscler. Thromb. A J. Vasc. Biol, vol. 12, no. 1, pp. 1–5, 1. 1992.

[11]. Hansen H, Lopata R, and de Korte CL, "Noninvasive Carotid Strain Imaging Using Angular Compounding at Large Beam Steered Angles: Validation in Vessel Phantoms," IEEE Trans. Med. Imaging, vol. 28, no. 6, pp. 872–880, 6. 2009. [PubMed: 19131297]

[12]. Hansen HHG, De Borst GJ, Bots ML, Moll F, Pasterkamp G, and De Korte CL, "Noninvasive compound ultrasound elastography for vulnerable plaque detection: in vivo validation," Eur. Heart J, vol. 34, no. suppl 1, pp. P258–P258, 8. 2013.

[13]. Hansen HHG, de Borst GJ, Bots ML, Moll FL, Pasterkamp G, and de Korte CL, "Compound Ultrasound Strain Imaging for Noninvasive Detection of (Fibro)Atheromatous Plaques: Histopathological Validation in Human Carotid Arteries," JACC Cardiovasc. Imaging, vol. 9, no. 12, pp. 1466–1467, 12. 2016. [PubMed: 27931528]

[14]. El Jalbout Ret al., "The value of non-invasive vascular elastography (NIVE) in detecting early vascular changes in overweight and obese children," Eur. Radiol, vol. 29, no. 7, pp. 3854–3861, 7. 2019. [PubMed: 30847591]

[15]. Schmitt C, Soulez G, Maurice RL, Giroux M-F, and Cloutier G, "Noninvasive Vascular Elastography: Toward A Complementary Characterization Tool of Atherosclerosis in Carotid Arteries," Ultrasound Med. Biol, vol. 33, no. 12, pp. 1841–1858, 12. 2007. [PubMed: 17698283]

[16]. Roy Cardinal M-Het al., "Carotid Artery Plaque Vulnerability Assessment Using Noninvasive Ultrasound Elastography: Validation With MRI," Am. J. Roentgenol, vol. 209, no. 1, pp. 142–151, 7. 2017. [PubMed: 28639927]

[17]. Poree J, Garcia D, Chayer B, Ohayon J, and Cloutier G, "Noninvasive Vascular Elastography With Plane Strain Incompressibility Assumption Using Ultrafast Coherent Compound Plane Wave Imaging," IEEE Trans. Med. Imaging, vol. 34, no. 12, pp. 2618–2631, 12. 2015. [PubMed: 26625341]

[18]. Garrard Jet al., "Shear Wave Elastography May Be Superior to Greyscale Median for the Identification of Carotid Plaque Vulnerability: A Comparison with Histology," Ultraschall der Medizin - Eur. J. Ultrasound, vol. 36, no. 04, pp. 386–390, 6. 2015.

[19]. V Ramnarine K, Garrard JW, Kanber B, Nduwayo S, Hartshorne TC, and Robinson TG, "Shear wave elastography imaging of carotid plaques: feasible, reproducible and of clinical potential," Cardiovasc. Ultrasound, vol. 12, no. 1, p. 49, 12. 2014. [PubMed: 25487290]

[20]. Bertrand-Grenier Aet al., "Abdominal aortic aneurysm follow-up by shear wave elasticity imaging after endovascular repair in a canine model Abbreviations AAA Abdominal aortic aneurysm CEUS Contrast-enhanced ultrasonography CI Confidence interval CT Computed tomography," Eur Radiol, vol. 27, pp. 2161–2169, 2017. [PubMed: 27572808]

[21]. Luo Jianwen, Li RX, and Konofagou EE, "Pulse wave imaging of the human carotid artery: an in vivo feasibility study," IEEE Trans. Ultrason. Ferroelectr. Freq. Control, vol. 59, no. 1, pp. 174–181, 1. 2012. [PubMed: 22293749]

[22]. Fujikura Ket al., "A Novel Noninvasive Technique for Pulse-Wave Imaging and Characterization of Clinically-Significant Vascular Mechanical Properties *In Vivo*," Ultrason. Imaging, vol. 29, no. 3, pp. 137–154, 7. 2007. [PubMed: 18092671]

[23]. Li RX, Luo J, Balaram SK, Chaudhry FA, Shahmirzadi D, and Konofagou EE, "Pulse wave imaging in normal, hypertensive and aneurysmal human aortas *in vivo*: a feasibility study," Phys. Med. Biol, vol. 58, no. 13, pp. 4549–4562, 7. 2013. [PubMed: 23770991]

[24]. Luo Jianwen, Fujikura K, Tyrie LS, Tilson MD, and Konofagou EE, "Pulse Wave Imaging of Normal and Aneurysmal Abdominal Aortas *In Vivo*," IEEE Trans. Med. Imaging, vol. 28, no. 4, pp. 477–486, 4. 2009. [PubMed: 19272985]

[25]. Apostolakis IZ, McGarry MDJ, Bunting EA, and Konofagou EE, "Pulse wave imaging using coherent compounding in a phantom and *in vivo*," Phys. Med. Biol, vol. 62, no. 5, pp. 1700–1730, 3. 2017. [PubMed: 28002039]

[26]. Apostolakis I-Z, Nauleau P, Papadacci C, McGarry MD, and Konofagou EE, "Feasibility and Validation of 4-D Pulse Wave Imaging in Phantoms and In Vivo," IEEE Trans. Ultrason. Ferroelectr. Freq. Control, vol. 64, no. 9, pp. 1305–1317, 9. 2017. [PubMed: 28792891]

[27]. Nauleau P, Apostolakis I, McGarry M, and Konofagou E, “Cross-correlation analysis of pulse wave propagation in arteries: In vitro validation and in vivo feasibility,” Phys. Med. Biol, vol. 63, no. 11, p. 115006, 5 2018. [PubMed: 29658889]

[28]. Karageorgos GM, Apostolakis IZ, Nauleau P, Weber R, and Konofagou EE, “Automated Spatial Mechanical Inhomogeneity Detection and Arterial Wall Characterization in Human Atherosclerotic Carotid Arteries In-Vivo,” in 2018 IEEE International Ultrasonics Symposium (IUS), 2018, pp. 1–9.

[29]. Pasterkamp G, de Kleijn DP, and Borst C, “Arterial remodeling in atherosclerosis, restenosis and after alteration of blood flow: potential mechanisms and clinical implications,” Cardiovasc. Res, vol. 45, no. 4, pp. 843–852, 3. 2000. [PubMed: 10728409]

[30]. Zarins CK, Giddens DP, Bharadvaj BK, Sottiurai VS, Mabon RF, and Glagov S, “Carotid bifurcation atherosclerosis. Quantitative correlation of plaque localization with flow velocity profiles and wall shear stress.,” Circ. Res, vol. 53, no. 4, pp. 502–14, 10. 1983. [PubMed: 6627609]

[31]. Lin GS and Naval VS, “Pattern of Doppler Flow Indices at the Carotid Bifurcation Evaluation by Hemodynamic Color Doppler Imaging,” 2001.

[32]. Middleton WD, Foley WD, and Lawson TL, “Flow reversal in the normal carotid bifurcation: color Doppler flow imaging analysis.,” Radiology, vol. 167, no. 1, pp. 207–10, 4. 1988. [PubMed: 2964676]

[33]. Gnasso Aet al., “In Vivo Association Between Low Wall Shear Stress and Plaque in Subjects With Asymmetrical Carotid Atherosclerosis,” Stroke, vol. 28, no. 5, pp. 993–998, 5 1997. [PubMed: 9158640]

[34]. Fadnes S, Ekroll IK, Nyrnes SA, Torp H, and Lovstakken L, “Robust angle-independent blood velocity estimation based on dual-angle plane wave imaging,” IEEE Trans. Ultrason. Ferroelectr. Freq. Control, vol. 62, no. 10, pp. 1757–1767, 10. 2015. [PubMed: 26470038]

[35]. Ekroll IK, Voormolen MM, Standal OK-V, Rau JM, and Lovstakken L, “Coherent compounding in doppler imaging,” IEEE Trans. Ultrason. Ferroelectr. Freq. Control, vol. 62, no. 9, pp. 1634–1643, 9. 2015. [PubMed: 26415126]

[36]. Dunmire B, Beach KW, Labs K-H, Plett M, and Strandness DE, “Cross-beam vector Doppler ultrasound for angle-independent velocity measurements,” Ultrasound Med. Biol, vol. 26, no. 8, pp. 1213–1235, 10. 2000. [PubMed: 11120358]

[37]. Yiu BYS and Yu ACH, “Least-Squares Multi-Angle Doppler Estimators for Plane-Wave Vector Flow Imaging,” IEEE Trans. Ultrason. Ferroelectr. Freq. Control, vol. 63, no. 11, pp. 1733–1744, 11. 2016. [PubMed: 27824557]

[38]. Udesen J, Gran F, Hansen K, Jensen JA, Thomsen C, and Nielsen MB, “High frame-rate blood vector velocity imaging using plane waves: Simulations and preliminary experiments,” IEEE Trans. Ultrason. Ferroelectr. Freq. Control, vol. 55, no. 8, pp. 1729–1743, 8. 2008. [PubMed: 18986917]

[39]. Kortbek J and Jensen J, “Estimation of velocity vector angles using the directional cross-correlation method,” IEEE Trans. Ultrason. Ferroelectr. Freq. Control, vol. 53, no. 11, pp. 2036–2049, 11. 2006. [PubMed: 17091840]

[40]. Trahey GE, Allison JW, and von Ramm OT, “Angle Independent Ultrasonic Detection of Blood Flow,” IEEE Trans. Biomed. Eng, vol. BME-34, no. 12, pp. 965–967, 12. 1987.

[41]. Jensen JA and Munk P, “A new method for estimation of velocity vectors,” IEEE Trans. Ultrason. Ferroelectr. Freq. Control, vol. 45, no. 3, pp. 837–851, 5 1998. [PubMed: 18244236]

[42]. Lenge M, Ramalli A, Tortoli P, Cachard C, and Liebgott H, “Plane-wave transverse oscillation for high-frame-rate 2-D vector flow imaging,” IEEE Trans. Ultrason. Ferroelectr. Freq. Control, vol. 62, no. 12, pp. 2126–2137, 12. 2015. [PubMed: 26670852]

[43]. Jensen JA, “Directional Transverse Oscillation Vector Flow Estimation,” IEEE Trans. Ultrason. Ferroelectr. Freq. Control, vol. 64, no. 8, pp. 1194–1204, 8. 2017. [PubMed: 28796606]

[44]. Katritsis D, Kaiktsis L, Chaniotis A, Pantos J, Efstathopoulos EP, and Marmarelis V, “Wall Shear Stress: Theoretical Considerations and Methods of Measurement,” Prog. Cardiovasc. Dis, vol. 49, no. 5, pp. 307–329, 3. 2007. [PubMed: 17329179]

[45]. Lenge M, Ramalli A, Cellai A, Tortoli P, Cachard C, and Liebgott H, “A new method for 2D-vector blood flow imaging based on unconventional beamforming techniques,” in ICASSP, IEEE International Conference on Acoustics, Speech and Signal Processing - Proceedings, 2014, pp. 5125–5129.

[46]. Luo J and Konofagou EE, “Imaging of Wall Motion Coupled With Blood Flow Velocity in the Heart and Vessels in Vivo: A Feasibility Study,” Ultrasound Med. Biol, vol. 37, no. 6, pp. 980–995, 6. 2011. [PubMed: 21546155]

[47]. Ekroll IK, Swillens A, Segers P, Dahl T, Torp H, and Lovstakken L, “Simultaneous quantification of flow and tissue velocities based on multi-angle plane wave imaging,” IEEE Trans. Ultrason. Ferroelectr. Freq. Control, vol. 60, no. 4, pp. 727–738, 4. 2013. [PubMed: 23549533]

[48]. Montaldo G, Tanter M, Bercoff J, Benech N, and Fink M, “Coherent plane-wave compounding for very high frame rate ultrasonography and transient elastography,” IEEE Trans. Ultrason. Ferroelectr. Freq. Control, vol. 56, no. 3, pp. 489–506, 3. 2009. [PubMed: 19411209]

[49]. Fekkes S, Saris AECM, Nillesen MM, Menssen J, Hansen HHG, and de Korte CL, “Simultaneous Vascular Strain and Blood Vector Velocity Imaging Using High-Frequency Versus Conventional-Frequency Plane Wave Ultrasound: A Phantom Study,” IEEE Trans. Ultrason. Ferroelectr. Freq. Control, vol. 65, no. 7, pp. 1166–1181, 7. 2018. [PubMed: 29993371]

[50]. Perrot V, “Ultrafast ultrasound imaging for simultaneous extraction of flow and arterial wall motion with linear array probe,” http://www.theses.fr, 10. 2019.

[51]. Perrot V, Liebgott H, Long A, and Vray D, “Simultaneous Tissue and Flow Estimation at High Frame Rate Using Plane Wave and Transverse Oscillation on in Vivo Carotid,” in IEEE International Ultrasonics Symposium, IUS, 2018, vol. 2018-October.

[52]. Perrot Vet al., “Translation of Simultaneous Vessel Wall Motion and Vectorial Blood Flow Imaging in Healthy and Diseased Carotids to the Clinic: a Pilot Study,” IEEE Trans. Ultrason. Ferroelectr. Freq. Control, pp. 1–1, 8. 2020.

[53]. Goudot Get al., “Carotid Stiffness Assessment With Ultrafast Ultrasound Imaging in Case of Bicuspid Aortic Valve,” Front. Physiol, vol. 10, p. 1330, 10. 2019. [PubMed: 31708797]

[54]. Nandlall SD and Konofagou EE, “Assessing the Stability of Aortic Aneurysms with Pulse Wave Imaging.,” Radiology, vol. 281, no. 3, pp. 772–781, 12. 2016. [PubMed: 27276242]

[55]. Li RXet al., “Pulse Wave Imaging in Carotid Artery Stenosis Human Patients in Vivo.,” Ultrasound Med. Biol, vol. 0, no. 0, 11. 2018.

[56]. Karageorgos GMet al., “Arterial wall mechanical inhomogeneity detection and atherosclerotic plaque characterization using high frame rate pulse wave imaging in carotid artery disease patients in vivo,” Phys. Med. Biol, vol. 65, no. 2, p. 16, 1. 2020.

[57]. Karageorgos GM, Apostolakis IZ, Nauleau P, Gatti V, Weber R, and Konofagou EE, “Atherosclerotic plaque mechanical characterization coupled with vector Doppler imaging in atherosclerotic carotid arteries in-vivo,” in Proceedings of the Annual International Conference of the IEEE Engineering in Medicine and Biology Society, EMBS, 2019, pp. 6200–6203.

[58]. Vittorio G, Nauleau P, Karageorgos GM, Shim J, Ateshian G, and Konofagou E, “Modelling pulse wave propagation through a stenotic artery with fluid structure interaction: a validation study using ultrasound pulse wave imaging,” Biomech. Model. Mechanobiol.

[59]. V Ramnarine K, Nassiri DK, Hoskins PR, and Lubbers J, “Validation of a New Blood-Mimicking Fluid for Use in Doppler Flow Test Objects,” Ultrasound Med. Biol, vol. 24, no. 3, pp. 451–459, 3. 1998. [PubMed: 9587999]

[60]. Maas SA, Ellis BJ, Ateshian GA, and Weiss JA, “FEBio: Finite Elements for Biomechanics,” J. Biomech. Eng, vol. 134, no. 1, 2. 2012.

[61]. Ateshian GA, Shim JJ, Maas SA, and Weiss JA, “Finite Element Framework for Computational Fluid Dynamics in FEBio,” J. Biomech. Eng, vol. 140, no. 2, p. 0210011, 2. 2018.

[62]. Nagaoka R, Masuno G, Kobayashi K, Yoshizawa S, Umemura S, and Saijo Y, “Measurement of regional pulse-wave velocity using spatial compound imaging of the common carotid artery in vivo,” Ultrasonics, vol. 55, pp. 92–103, 1. 2015. [PubMed: 25152379]

[63]. Hasegawa H, Hongo K, and Kanai H, “Measurement of regional pulse wave velocity using very high frame rate ultrasound,” J. Med. Ultrason, vol. 40, no. 2, pp. 91–98, 4. 2013.

[64]. Huang C, Su Y, Zhang H, Qian L-X, and Luo J, “Comparison of Different Pulse Waveforms for Local Pulse Wave Velocity Measurement in Healthy and Hypertensive Common Carotid Arteries in Vivo,” Ultrasound Med. Biol, vol. 42, no. 5, pp. 1111–1123, 5 2016. [PubMed: 26924694]

[65]. Demene Cet al., “Spatiotemporal Clutter Filtering of Ultrafast Ultrasound Data Highly Increases Doppler and fUltrasound Sensitivity,” IEEE Trans. Med. Imaging, vol. 34, no. 11, pp. 2271–2285, 11. 2015. [PubMed: 25955583]

[66]. Tsang IKH, Yiu BYS, and Yu ACH, “A least-squares vector flow estimator for synthetic aperture imaging,” in 2009 IEEE International Ultrasonics Symposium, 2009, pp. 1387–1390.

[67]. Karageorgos GMet al., “Imaging of pulse wave propagation coupled with vector flow and wall shear stress mapping in atherosclerotic plaque phantoms and in vivo,” in IEEE International Ultrasonics Symposium, IUS, 2019, vol. 2019-October, pp. 243–246.

[68]. Lee Wei-Ning, Ingrassia CM, Fung-Kee-Fung SD, Costa KD, Holmes JW, and Konofagou EE, “Theoretical Quality Assessment of Myocardial Elastography with In Vivo Validation,” IEEE Trans. Ultrason. Ferroelectr. Freq. Control, vol. 54, no. 11, pp. 2233–2245, 11. 2007. [PubMed: 18051158]

[69]. Konofagou E and Ophir J, “A new elastographic method for estimation and imaging of lateral displacements, lateral strains, corrected axial strains and Poisson’s ratios in tissues,” Ultrasound Med. Biol, vol. 24, no. 8, pp. 1183–1199, 10. 1998. [PubMed: 9833588]

[70]. Newhouse VL, Varner LW, and Bendick PJ, “Communications: Geometrical Spectram Broadening in Ultrasonic Doppler Systems,” IEEE Trans. Biomed. Eng, vol. BME-24, no. 5, pp. 478–480, 1977.

[71]. Avdal J, Løvstakken L, Torp H, and Ekroll IK, “Combined 2-D Vector Velocity Imaging and Tracking Doppler for Improved Vascular Blood Velocity Quantification,” IEEE Trans. Ultrason. Ferroelectr. Freq. Control, vol. 64, no. 12, pp. 1795–1804, 12. 2017. [PubMed: 28961109]

[72]. Swillens A, Segers P, Torp H, and Løvstakken L, “Two-dimensional blood velocity estimation with ultrasound: Speckle tracking versus crossed-beam vector doppler based on flow simulations in a carotid bifurcation model,” IEEE Trans. Ultrason. Ferroelectr. Freq. Control, vol. 57, no. 2, pp. 327–339, 2. 2010. [PubMed: 20178899]

[73]. Hoyos CAV, Stuart MB, Hansen KL, Nielsen MB, and Jensen JA, “Accurate Angle Estimator for High-Frame-Rate 2-D Vector Flow Imaging,” IEEE Trans. Ultrason. Ferroelectr. Freq. Control, vol. 63, no. 6, pp. 842–853, 6. 2016. [PubMed: 27093598]

[74]. Jensen J, Hoyos CAV, Stuart MB, Ewertsen C, Nielsen MB, and Jensen JA, “Fast Plane Wave 2-D Vector Flow Imaging Using Transverse Oscillation and Directional Beamforming,” IEEE Trans. Ultrason. Ferroelectr. Freq. Control, vol. 64, no. 7, pp. 1050–1062, 7. 2017. [PubMed: 28422656]

[75]. Kung EO and Taylor CA, “Development of a Physical Windkessel Module to Re-Create In Vivo Vascular Flow Impedance for In Vitro Experiments,” Cardiovasc. Eng. Technol, vol. 2, no. 1, pp. 2–14, 3. 2011. [PubMed: 26316899]

[76]. Rahman Rasyada A and Azhim A, “Flow Velocity in Common Carotid Artery,” in Carotid Artery - Gender and Health [Working Title], IntechOpen, 2018.

[77]. Irace Cet al., “Human common carotid wall shear stress as a function of age and gender: a 12-year follow-up study,” Age (Omaha)., vol. 34, no. 6, pp. 1553–1562, 12. 2012.

[78]. Gnasso Aet al., “Association Between Intima-Media Thickness and Wall Shear Stress in Common Carotid Arteries in Healthy Male Subjects,” Circulation, vol. 94, no. 12, pp. 3257–3262, 12. 1996. [PubMed: 8989138]

[79]. Samijo SKet al., “Wall shear stress in the human common carotid artery as function of age and gender,” Cardiovasc. Res, vol. 39, no. 2, pp. 515–522, 8. 1998. [PubMed: 9798536]

[80]. Lee H-Y and Oh B-H, “Aging and Arterial Stiffness,” Circ. J, vol. 74, no. 11, pp. 2257–2262, 2010. [PubMed: 20962429]

[81]. Kochanowicz J, Mariak Z, Rutkowski R, Turek G, Lysoń T, and Krejza J, “Age and sex dependency of blood flow velocity in the internal carotid artery.,” Neurol. Neurochir. Pol, vol. 43, no. 1, pp. 3–8, 2009. [PubMed: 19353438]

[82]. Duivenvoorden Ret al., “Endothelial Shear Stress A Critical Determinant of Arterial Remodeling and Arterial Stiffness in Humans-A Carotid 3.0-T MRI Study,” 2010.

[83]. Leow CH and Tang MX, “Spatio-Temporal Flow and Wall Shear Stress Mapping Based on Incoherent Ensemble-Correlation of Ultrafast Contrast Enhanced Ultrasound Images,” Ultrasound Med. Biol, vol. 44, no. 1, pp. 134–152, 1. 2018. [PubMed: 29037843]

[84]. Mcgarry M, Li R, Apostolakis I, Nauleau P, and Konofagou EE, “An inverse approach to determining spatially varying arterial compliance using ultrasound imaging.,” Phys. Med. Biol, vol. 61, no. 15, pp. 5486–507, 2016. [PubMed: 27384105]

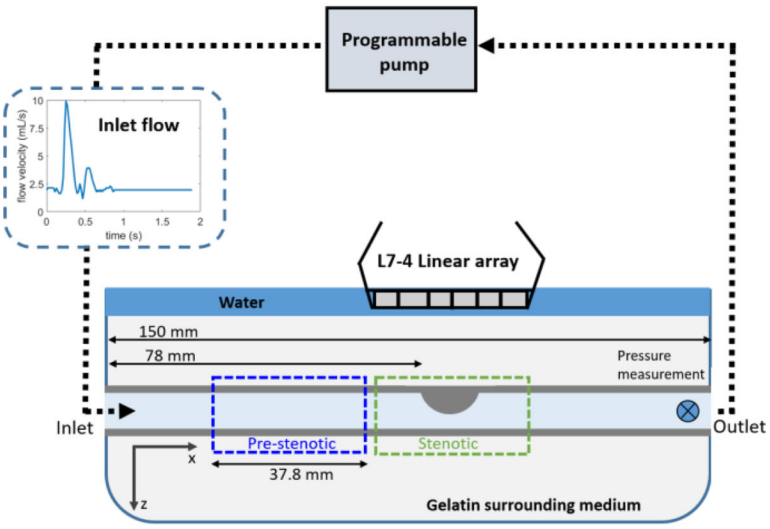

Figure 1:

Phantom experimental setup. A PVA phantom, mimicking an atherosclerotic vessel with 50% stenosis is connected to a programmable pump, which generates a physiological carotid artery flow waveform. The blue and green rectangles illustrate the different sites where the phantom was scanned

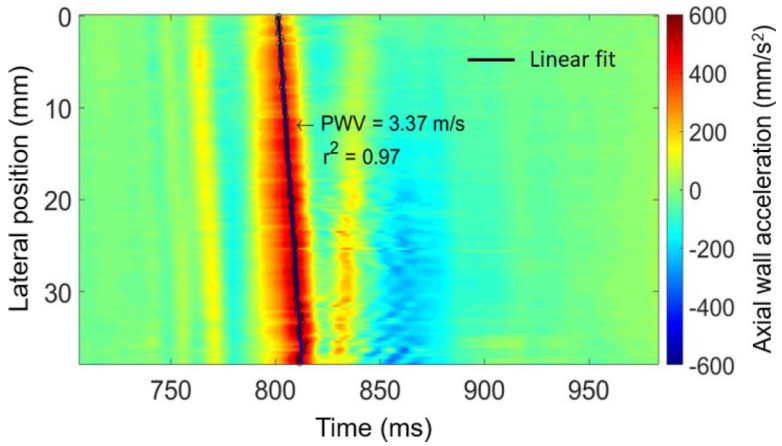

Figure 2:

Acceleration spatiotemporal plot with linear fit overlaid for pulse wave tracking and PWV estimation.

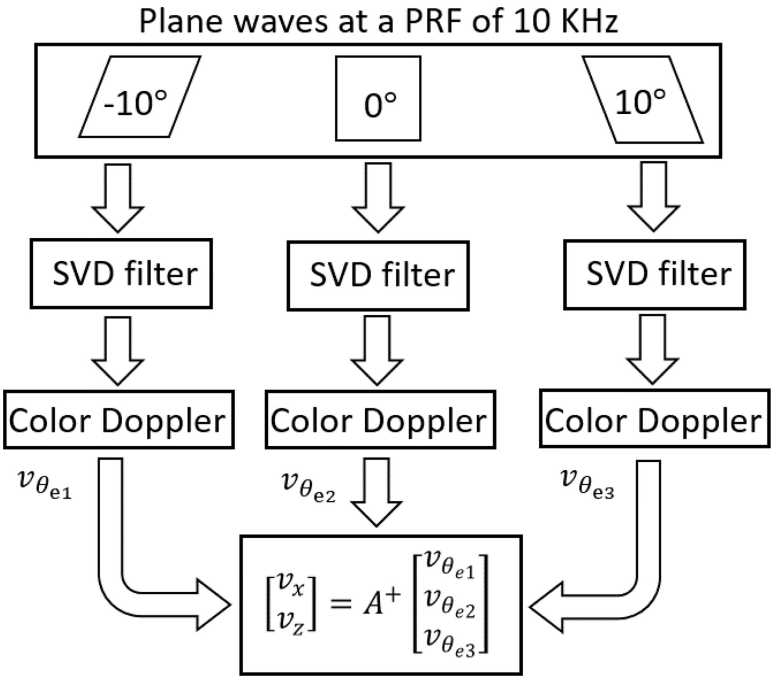

Figure 3:
Vector Doppler methodology

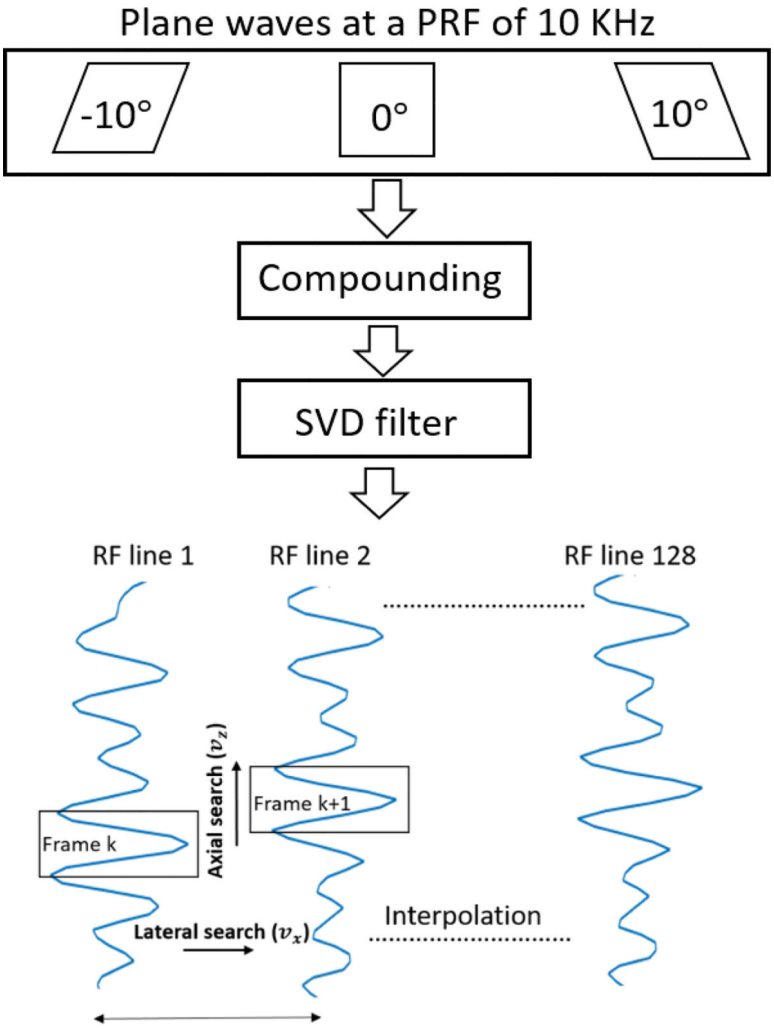

Figure 4:
Cross correlation vector flow imaging methodology

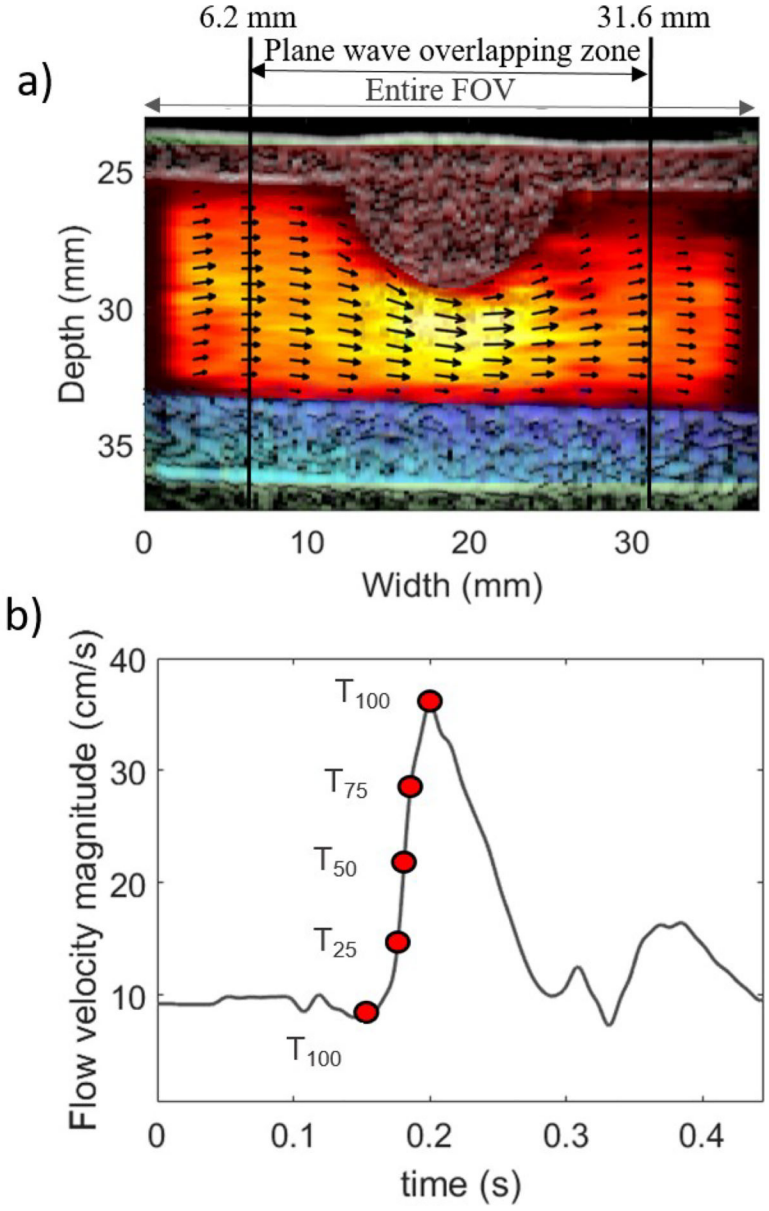

Figure 5:

(a) Borders of plane wave overlapping zone and entire field of view, in which the average bias and precision values were calculated. (b) Points of the flow velocity waveform for which the bias and precision values were calculated.

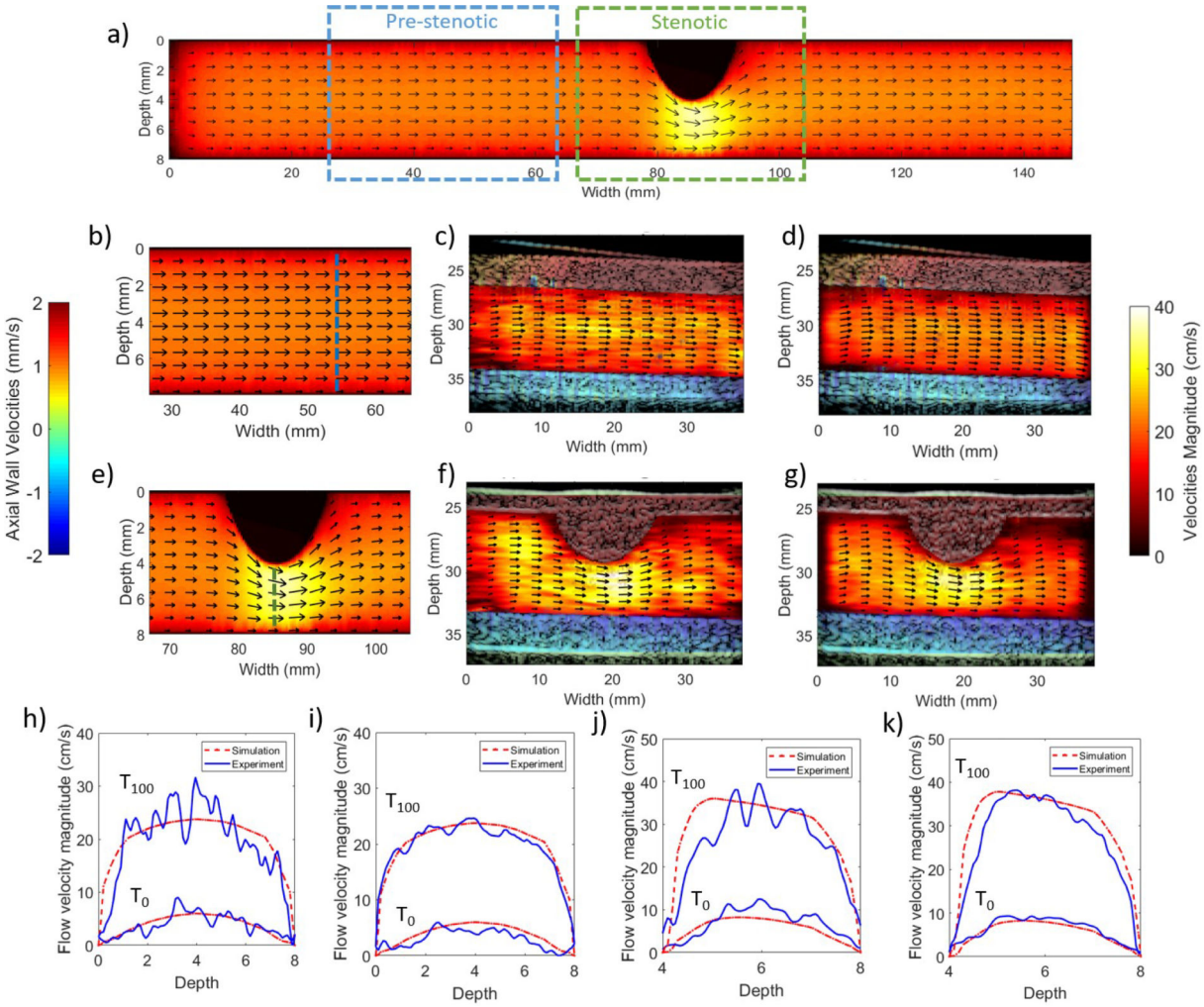

Figure 6:

(a) 2-D flow vector field at the time frame of peak systole (T_{100}), corresponding to the central 2-D slice of the phantom's geometry, as obtained through FSI simulation. The blue and green rectangles denote the segments of the phantom where ultrasound scans were performed. (b-g) Peak systolic vector flow field, before interpolation, obtained through simulation, vector Doppler and CC VFI in the pre-stenotic (b,c,d) and stenotic (e,f,g) segment, respectively. (h-k) Axial flow velocity magnitude profiles, after interpolation, at the foot (T_0) and peak (T_{100}) time frames as obtained through vector Doppler (h,j) and CC VFI (i,k), in the pre-stenotic (h,i) and stenotic (j.k) segment, respectively.

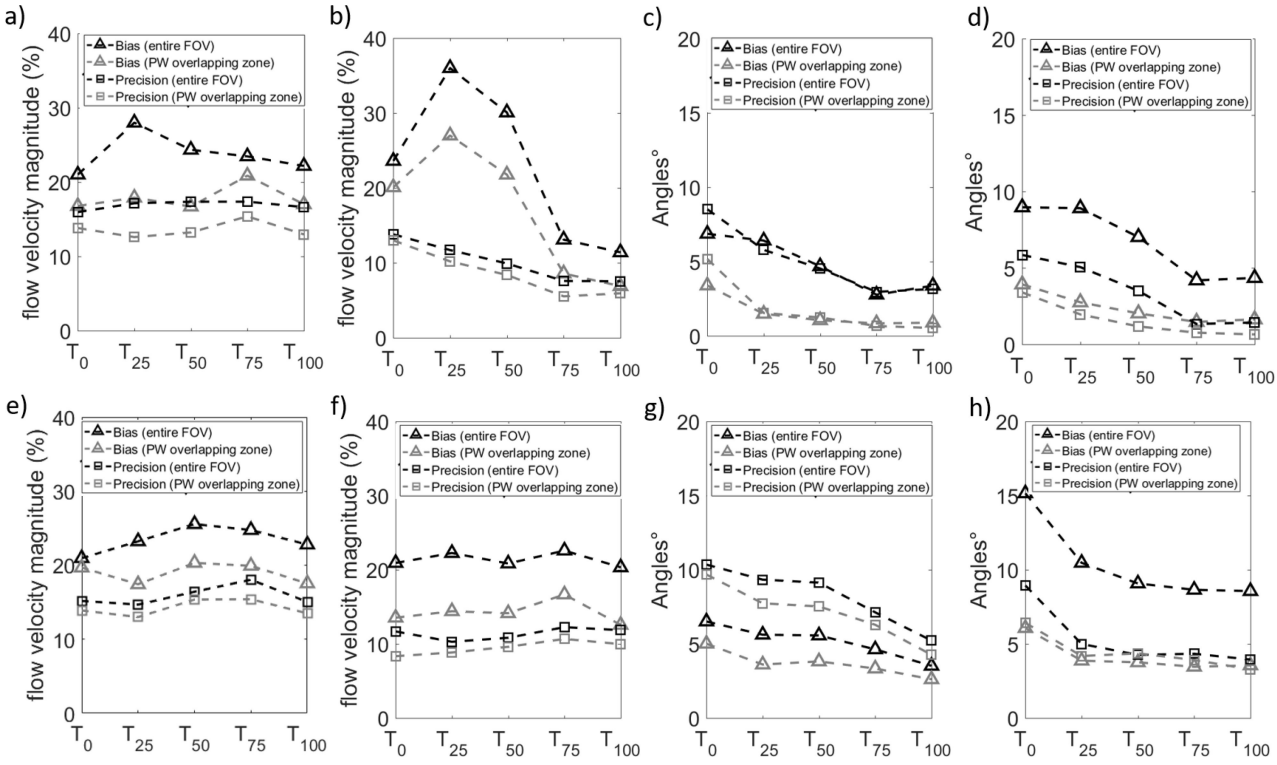

Figure 7:

Bias and precision in flow velocity magnitude (a, b, e, f) and vector angles (c, d, g, h), with respect to the time frame in the pre-stenotic (a - d) and stenotic (e - h) segments. (a,c,e,g) illustrate the values obtained through the vector Doppler technique. (b,d,f,h) illustrate the values obtained through the CC-VFI technique.

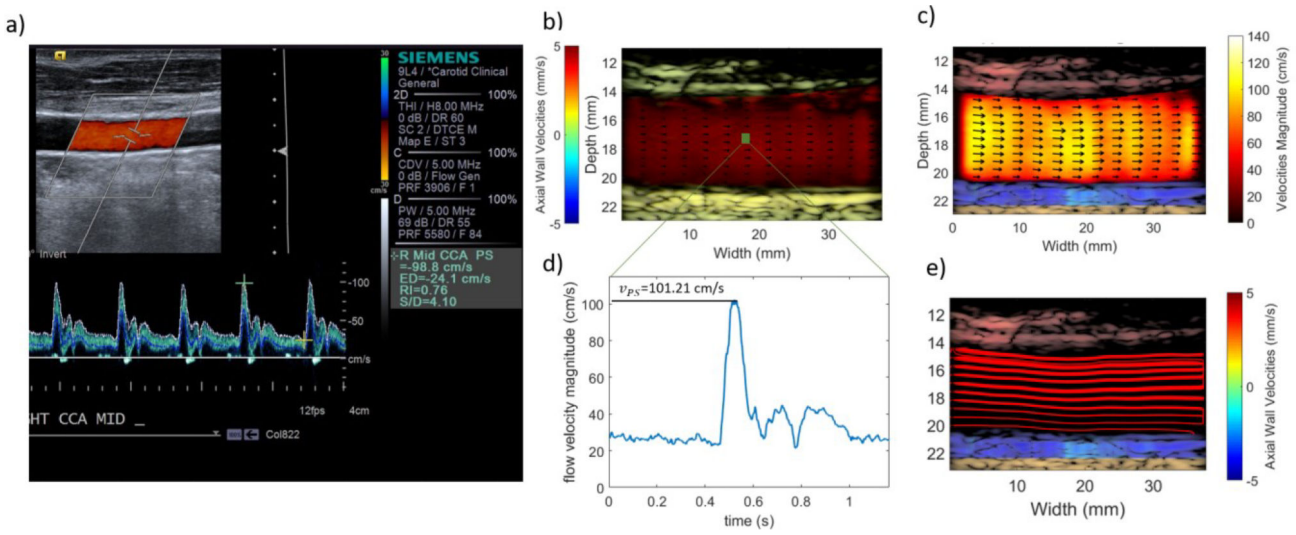

Figure 8:

(a) Pulsed wave Doppler scan provided by a clinical ultrasound scanner. (b,c) Images of PWI combined with CC-VFI imaging sequence corresponding to end diastole and peak systole, respectively. (d) Temporal waveform of flow velocity magnitude, as obtained through CC VFI, corresponding to the center of the lumen (green rectangular marker in Figure 8–(b)), which is the approximate location of the PW Doppler measurement. (e) An alternative display of the proposed method, in which streamlines are plotted onto the B-mode in order to provide improved visualization of the directional flow in the common carotid.

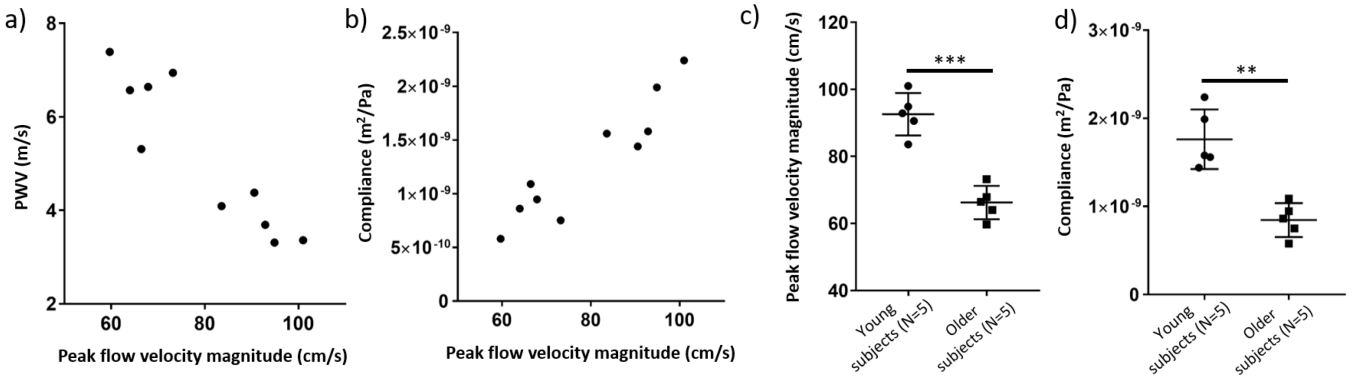

Figure 9:

(a) PWV and (c) Compliance versus peak flow velocity magnitude averaged throughout the arterial lumen. Comparison of (c) peak flow velocity magnitude and (d) compliance in young and older subjects.

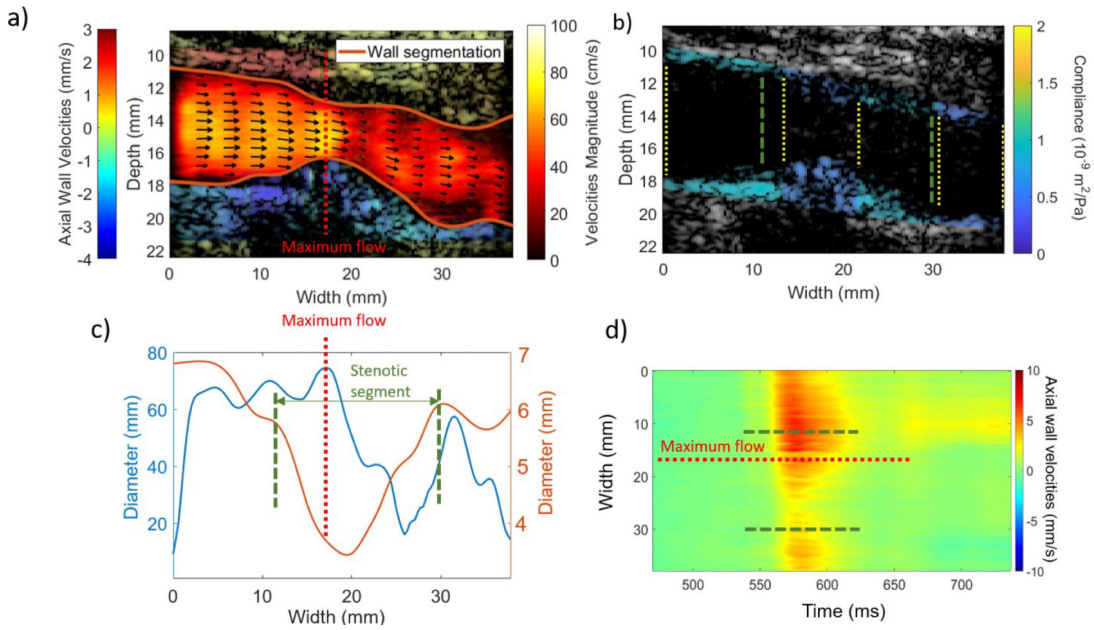

Figure 10:

(a) B-mode image with the flow magnitude and vector field overlaid inside the lumen and the axial wall velocities overlaid on the walls. The orange lines depict the borders of the lumen, obtained through manual wall segmentation. (b) Output of the adaptive PWI method. The yellow dashed lines indicate the borders of most homogeneous segments detected by adaptive PWI, while the compliance values are color-coded and overlaid onto the B-mode. The green dashed lines correspond to the borders of the stenotic segment, as determined by lumen diameter analysis. (c) Peak flow magnitude with respect to the lateral position, in a common graph with the lumen diameter, as obtained through wall segmentation. The vertical red dashed line indicates the lateral position where the flow magnitude maximizes, while the green lines indicate the borders of the stenotic segment as determined through the diameter waveform. (d) Spatiotemporal plot of arterial distension rate.

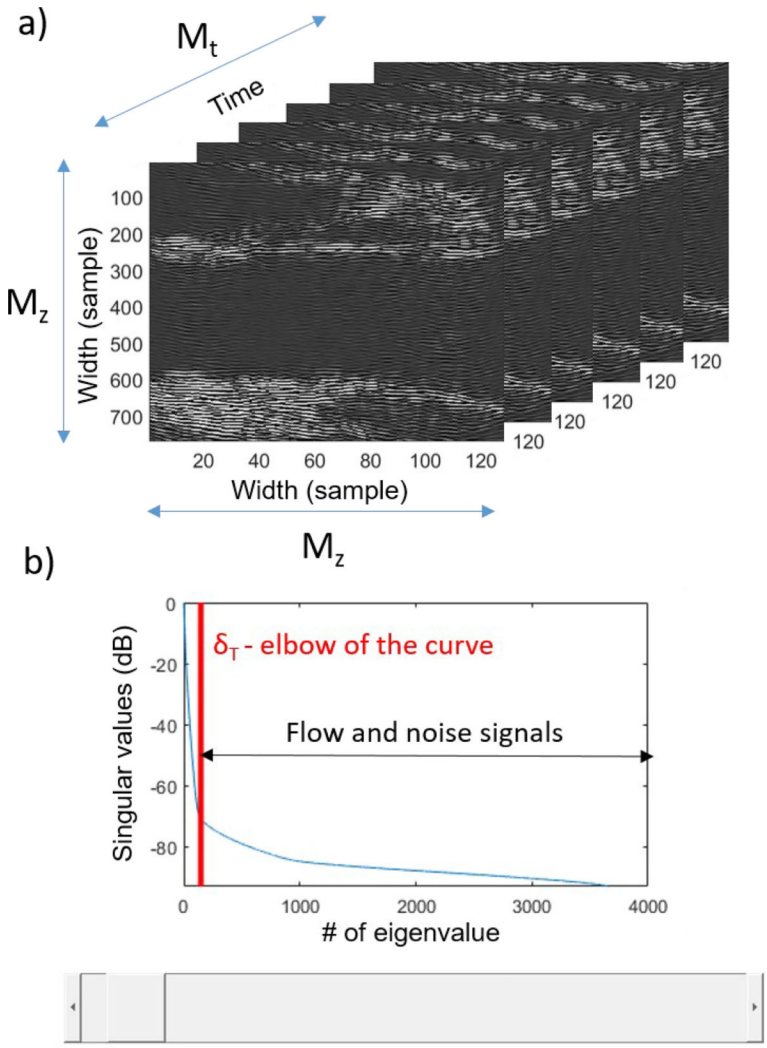

Figure 11:

(a) 3-D stack of beamformed RF frames. (b) User interactive GUI for singular value filtering threshold selection.

TABLE I –

ULTRASOUND ACQUISITION PARAMETERS

System	**Verasonics Vantage 256**
Transducer type	128-element linear array
Center frequency	5MHz
Element pitch	0.298 mm
Field of View	35mm×37.88mm
PRF	10000Hz
RF sampling rate	20MHz
Pulse length	2 cycles
Acquisition duration	1.2 s
Transmit apodization	No apodization

TABLE II –

Average bias and precision values obtained for each scanning site and each vector flow imaging technique

	Pre-stenotic segment		Stenotic segment	
	Vector Doppler	**CC VFI**	**Vector Doppler**	**CC VFI**
B_{v_m}(%)	17.85±1.74	16.36±7.96	18.96±1.38	14.26±1.51 *
B_θ(°)	1.53±1.06 *	2.35±1.00	4.21 ±1.12	4.14±1.08
σ_{v_m}(%)	13.59±1.09	8.61±3.10 *	14.22±1.09	9.49±0.91 *
σ_θ(°)	1.83±1.91	1.58±1.13	7.10±1.99	4.43±1.18 *

* Significantly lower value ($p<0.05$)